Liquid-Mix Disorder in Crystalline Solids: ScMnO₃

Pavel Karen

Department of Chemistry, University of Oslo, P.O. Box 1033 Blindern, 0315 Oslo, Norway

and

Patrick M. Woodward*

Physics Department, Brookhaven National Laboratory, Upton, New York 11973

The liquid-mix citrate synthesis of $ScMnO_3$, when conducted at temperatures below approximately 700°C, leads to the formation of a (nano)crystalline oxide with the liquid-mix disorder of the metal atoms preserved. The disordered phase has an excess of oxygen atoms over three per formula, implying the presence of both Mn^{3+} and Mn^{4+}. Synchrotron X-ray powder diffraction reveals two phases (domains) with nearly identical lattices in the liquid-mix sample; a bixbyite-type phase (as adopted by Sc_2O_3 and Mn_2O_3) and a defect fluorite-type phase. Examinations of the unit-cell parameters indicate that most if not all of the Mn^{4+} and excess oxygen are incorporated into the fluorite-type phase. Annealing at temperatures higher than 700°C induces a rapid transformation of this phase mixture into a single-phase product represented by the stable hexagonal modification of $ScMnO_3$. Both components of the liquid-mix oxide, viz. the metastable bixbyite-type phase and the oxidation-stabilized fluorite-type phase, exhibit high strain attributed to the size imbalance of the constituent metal atoms. Transformation into the stable ordered hexagonal phase is accompanied by an order of magnitude decrease in the micro-strain and a dramatic increase in the crystallite size. The kinetics of the ordering phase transition have been investigated using conventional X-ray powder diffraction techniques. Disordered $(Sc_{1-x}Mn_x)_2O_{3+\delta}$ solid solutions, synthesized analogously by the liquid-mix technique, transform under exsolution of $ScMnO_3$ into stable solid solutions. The thermodynamically stable solid-solution limits are estimated to be $(Sc_{0.85}Mn_{0.15})_2O_3$ and $(Sc_{0.10}Mn_{0.90})_2O_3$ at 1000°C for the scandium and manganese rich ends of the phase diagram, respectively. © 1998 Academic Press

Key Words: scandium manganese oxide; liquid-mix disorder; metastable; ordering kinetics; synchrotron X-ray diffraction; crystallite size; micro-strain analysis.

*Present address: Department of Chemistry, Ohio State University, Newman and Wolfrom Laboratory, 100 West 18th Avenue, Columbus, OH 43210.

I. INTRODUCTION

Liquid-mix syntheses of solid-state inorganic oxides are powerful techniques greatly diminishing the diffusion distances otherwise necessary when conventional powder-mix techniques are used (1). Perhaps (chemically) the most universal of these methods are those originating from citrates, either based on citrate-ethyleneglycol polymers (2) or on melted hydrated citrates (3), which do not rely on internal combustion to obtain the solid precursor. In particular, the latter method leads to low contents of the organic binder in the precursor, and this allows for a very slow incineration at relatively low temperatures approaching "soft chemistry" conditions (4) with diffusion-limited crystallization. Numerous reports of occurrence of metastable phases stabilized by a kinetic barrier under various precursor syntheses have been communicated, as an example, Refs. (4–6).

The chemistry of the Sc(O)–Mn(O) phase system (7) is dominated by the redox properties of Mn. However, trivalent Mn occurs over a wide range of temperatures and oxygen partial pressures (7, 8). The cubic, bixbyite-type structure is adopted by the trivalent oxides Sc_2O_3 (9) and Mn_2O_3 above 29°C (10, 11), but their mutual solid miscibility (7) is rather limited. One intermediate phase is formed in this subsystem, $ScMnO_3$. This compound has a hexagonal crystal structure and is reported to be isostructural with ferroelectric $LuMnO_3$ (12, 13). Under high pressures, a $Sc_2Mn_2O_7$ pyrochlore-type phase is formed with tetravalent Mn (14, 15).

In this paper, formation of $ScMnO_3$ with the liquid-mix-induced disorder of the metal atoms is reported, and its ordering into the stable high-temperature modification is studied by conventional and synchrotron X-ray powder diffraction (XRPD) techniques.

II. EXPERIMENTAL

Liquid-Mix Syntheses

The samples were synthesized by the liquid-mix method in melted hydrated citrates (3). Formates of Sc and Mn were chosen as starting materials, synthesized by dissolution of the reagent-grade Sc_2O_3 and $MnCO_3$, respectively, in hot $1 + 1$ aqueous solutions of formic acid followed by iso-plethal crystallizations. The $Sc(HCOO)_3$ and $Mn(HCOO)_2 \cdot 2H_2O$ compositions were verified by complexometric titrations with EDTA. An aqueous solution of the two formates in desired proportion, having a metals concentration of approximately 0.5 mol/L in sum, was slowly added to the melted citric acid monohydrate (reagent-grade, Merck). The amount of 10 moles of citric acid per 1 mole of metals was tested to be high enough to prevent precipitations of citrates or basic citrates of Sc and Mn. A citrate melt with a honey consistency was formed upon evaporation of water and most of the formic acid. Further heat treatment at $180°C$ in air led to a continued removal of water and of the excessive organic matter resulting in the formation of a yellow-brown solid foam of the organic precursor. This temperature also defined the final ratio of the metals to the organics, as manifested by the cessation of the development of the acrid vapours formed from the decomposition products of citric acid. Porcelain crucibles were filled up with the finely powdered organic precursor (~ 3 g; milled in a vibration agate mill), covered with a lid, and heated over the period of 2 days in air at $450°C$. The slow incineration produced a nanoscale inorganic precursor which was subsequently pressed into pellets (160 kg/cm^2) and annealed for 48 h at $690°C$ in pure O_2, followed by a free cooling inside the furnace. In this manner, liquid-mix solid solution samples of $(Sc_{1-x}Mn_x)_2O_3$ have been obtained for $x = 0.20, 0.40, 0.60, 0.80$, as well as for $x = 0.5$ ($ScMnO_3$).

Powder-Mix Syntheses

As a reference method for the synthesis of the $ScMnO_3$ composition, a standard ceramic powder-mix technique was tested at temperatures corresponding to the liquid-mix syntheses. Formates of Mn and Sc were used as the microscale powder precursors. Stoichiometric amounts of $Sc(HCOO)_3$ and $Mn(HCOO)_2 \cdot 2H_2O$ (~ 2 g in sum) were milled together, dried in a porcelain crucible at $170°C$ for 4 h and decomposed at $450°C$ over the period of 15 h. The resulting powder was milled (agate vibration mill) pressed into pellets and annealed two times for 60 h at $706°C$ with intermittent rehomogenization. This procedure merely gave a mixture of the two binary oxides, Sc_2O_3 with $a = 9.844(6)$ Å and Mn_2O_3 with $a = 9.412(4)$ Å.

Conventional XRPD

Guinier–Hägg focusing camera was used with Cu $K\alpha_1$ radiation and Si as an internal standard. The photographs were scanned by a LS-18 film scanner with software (16) for XRPD data treatment. Rough estimates of the content of the occurring chemical phases were obtained from observed and calculated (17) intensities of the 112 Bragg reflection for the hexagonal $ScMnO_3$ and 222,332 Bragg reflections for the bixbyite-type phase (18). Only stoichiometric values of the oxygen content were considered in the calculations.

Chemical Analyses

The oxidation state of Mn was determined iodometrically. The samples were digested in 6 M HCl with an excess of KI in glass ampoules sealed under Ar, accompanied by the redox reaction (I_3^- formation omitted):

$$2Mn^{v+} + 2(v-2)I^- = 2Mn^{2+} + (v-2)I_2. \quad [1]$$

Blank experiments were performed to account for the trace amount of I_2 that forms in the absence of the sample under the digestion conditions. The digestions lasted typically some 5 min at $\sim 60°C$ and were followed by titration by potassium thiosulphate (0.1 M solution, Merck) standardized on dried KIO_3 (titration standard, Merck). The titrated solution was then used for a subsequent complexometric titration of Mn or Sc.

The content of the metals in some samples was determined complexometrically by EDTA (0.05 M disodium salt; Merck), after dissolution in warm diluted hydrochloric acid. Scandium was titrated at pH ≈ 3 adjusted by hexamethylenetetraamine with Xylenol Orange as an indicator, manganese in a pH $= 10$ buffer with Eriochrome Black T as an indicator, and it was stabilized in the divalent state by small additions of hydroxylamine hydrochloride and triethyleneglycole.

Synchrotron XRPD

High-resolution synchrotron XRPD data were collected on the X7A beamline at the National Synchrotron Light Source (NSLS) at Brookhaven National Laboratory (BNL). The samples were sealed into 0.4-mm diameter glass capillaries which were freely rotated at speeds of 1–2 Hz during data collection to reduce any possible preferred orientation or texture effects. Monochromatic radiation ($\lambda = 0.70128$ Å) was obtained from a channel-cut double-crystal Si (111) monochromator. A linear position-sensitive detector (19) (PSD) was employed. The PSD, which can collect $6°$ of data at each step, was stepped in $0.25°$ intervals with counting times varying from 20 to 60 s per step. Rietveld refinements were performed using the GSAS software suite (20). Peak widths and positions, for the peak broadening analysis, were determined using the local software package GPLSFT. This package uses a least squares algorithm to fit peak profiles, using a pseudo-Voigt function corrected for asymmetry.

III. RESULTS AND DISCUSSION

A. Syntheses

The main factors controlling the compositions of the liquid-mix based samples are temperature, partial pressure of oxygen and time, the latter owing to the generally non-equilibrium situation. With p_{O_2} given by the chemical surroundings (O_2, air, atmosphere during the combustions), temperature seems to be the determining factor, as the changes, once allowed by the kinetics, occur rather rapidly.

Inorganic Precursors; 450°C

The precursors for $(Sc_{1-x}Mn_x)_2O_3$ ($x = 0.2, 0.4, 0.6, 0.8$) are nanopowders of a light to dark brown colour deepening with increasing x. When touched, the precursor powders easily dust, but can be cold-pressed into $\sim 15\%$ of their approximate X-ray density under 160 kg/cm² (1-mm thickness). According to XRPD, the powders are completely amorphous for the $x = 0.4$ and 0.6 compositions. The $x = 0.2$ sample shows a weak and broadenend pattern of a fluorite type (a bixbyite substructure), the $x = 0.8$ composition has a less broadened pattern of a spinel type. This extreme peak broadening observed in the diffraction patterns of these samples can be attributed to small crystallite size and/or micro-strain. If one neglects the strain present in these cubic samples, the volume-weighted crystallite size follows from the Scherrer formula (21, 22):

$$D_v = \frac{\lambda}{\beta_{size} \cos \Theta} \qquad [2]$$

where β_{size} is the integral breadth of a Bragg peak located at 2Θ (in radians 2Θ; integral breadth is the peak area divided by peak height) corrected for the broadening caused by the instrumental setup of the diffraction experiment. In terms of the full-width-at-half-maximum Γ, a Lorentzian peak shape has an integral breadth of $\beta = (\pi/2)\Gamma$, and for a Gaussian peak shape $\beta = [\pi/(4\ln 2)]^{1/2}\Gamma$ (23). For scanned Guinier–Hägg photographs, the peak shape is considered (24) to be Lorentzian. Although the assumption of negligible strain is not strictly valid in these samples (see Section III.C.3) the quality of the data did not warrant a more sophisticated analysis. Nonetheless, analysis using Eq. (2) in this situation is sufficient for a qualitative comparison of the changes in the crystallite size, D_v. In this analysis, Γ is corrected for the instrumental broadening estimated from the 111 reflection of Si. The 111 fluorite-type (equivalent to 222 bixbyite-type) and 113 spinel-type reflections in the scanned film photographs are used for the evaluations, giving $D_v = 50$ Å and $D_v = 70$ Å for the precursor samples $x = 0.2$ and $x = 0.8$, respectively.

TABLE 1
Compositions of the Inorganic Precursors According to Chemical Analyses

x	δ	$v(Mn)$	$w(oxide)$	$n(CO_2)$	$n(H_2O)$
0.20	0.061(3)	3.307(5)	0.862(3)	0.52(1)	1.27(3)
0.40	0.158(1)	3.395(2)	0.889(1)	0.422(1)	1.03(1)
0.60	0.10(1)	3.16(1)	0.930(3)	0.26(1)	0.64(3)
0.80	− 0.06(2)	2.93(3)	0.93(3)	0.25(11)	0.60(27)

Note. Mass fractions $w(oxide)$, of $(Sc_{1-x}Mn_x)_2O_{3+\delta}$ and moles of residual CO_2, or, alternatively, H_2O, are listed per this formula unit. Standard deviations are given in parentheses.

Chemical analyses have been carried out to shed some light on the compositions of the inorganic precursors and the results are listed in Table 1. It is seen that the pure-oxide content accounts for 86 to 93 wt% of the precursor samples, and the rest is assumed to represent residual carbonate and/or hydroxide ions, both bulk and surface. According to the chemical analyses, the oxidation state of Mn has a maximum at low Mn contents where it exceeds significantly + 3, for both the bixbyite-type $x = 0.20$ and the completely amorphous $x = 0.40$ sample. When the Mn content is high, the moderately reducing conditions under the incineration of the organic precursor decrease the Mn valence and a spinel-type structure with diffraction pattern of the Mn_3O_4 type is formed.

Liquid-Mix Solid Solutions; 690°C

These samples, obtained from the precursor under 48-h annealings in O_2, are all crystalline with Bragg reflections broadened, in particular on the Sc-rich side (Table 2). This broadening is assumed to reflect the small yet increasing particle size, as compared to the precursors. Conventional XRPD patterns indicate that the structure type of the end members Sc_2O_3 and Mn_2O_3 is adopted throughout all compositions. This apparent complete solid miscibility is not seen under equilibrium conditions in the phase-diagram study in Ref. (7). Chemical analyses (Table 3) show that the

TABLE 2
Mean Crystallite Size D_v (in Å) of the Liquid-Mix Bixbyite-Type Solid Solutions $(Sc_{1-x}Mn_x)_3O_{3+\delta}$

t (°C)	$x = 0.20$	$x = 0.40$	$x = 0.60$	$x = 0.80$
690	60	110	170	380
750	100	140		
850	290			

Note. Values were estimated using Eq. [2] and assuming single-phase samples with a Lorentzian peak shape.

TABLE 3
Compositions of the Liquid-Mix Solid Solutions (Obtained at 690°C) According to Chemical Analyses

x	δ	$v(Mn)$	w(oxide)	$n(CO_2)$	$n(H_2O)$
0.20	0.067(4)	3.34(2)	0.92(1)	0.27(6)	0.67(14)
0.40	0.110(3)	3.28(1)	0.967(4)	0.12(2)	0.28(4)
0.60	0.233(1)	3.388(1)	0.972(1)	0.100(1)	0.244(3)
0.80	0.050(14)	3.06(2)	0.986(4)	0.05(1)	0.13(3)

Note. Mass fractions w(oxide), of $(Sc_{1-x}Mn_x)_2O_{3+\delta}$ and moles of residual CO_2, or, alternatively, H_2O, are listed per this formula unit.

TABLE 4
Exsolution of Hexagonal $ScMnO_3$ from Cubic Liquid-Mix $(Sc_{1-x}Mn_x)_2O_{3+\delta}$ at Temperature t under a 48-h Annealing in 1 atm O_2: Estimated Mass Fractions

t (°C)	$x = 0.20$		$x = 0.40$		$x = 0.60$		$x = 0.80$	
	Cubic	$ScMnO_3$	Cubic	$ScMnO_3$	$ScMnO_3$	Cubic	$ScMnO_3$	Cubic
690	1.00		1.00		1.00		1.00	
750	1.00		1.00		0.46[a]	0.54[a]	0.08	0.92
1850	1.00		0.28	0.72	0.79	0.21	0.24	0.76
1000	0.89	0.11	0.26	0.74	0.78	0.22	0.21	0.79

[a] A small amount of the original liquid-mix solid solution is seen ($a = 9.59$ Å).

pure-oxide content is 92–99 wt%, i.e., higher than in the precursor, and increasing with increasing Mn content. The maximum in the Mn oxidation state attains approximately the same level as observed in the precursor samples, but it shifts to higher Mn contents around $x = 0.60$. This is also reflected in the color of that sample being the darkest. The $x = 0.8$ sample is close to trivalent Mn and so is the control sample of Mn_2O_3, obtained from decomposition of the formate at 900 °C in air and having $v(Mn) = 3.006(2)$.

At this point it should be noted that high-resolution synchrotron XRPD, performed for time constraints only on samples of the $ScMnO_3$ composition (see Section III.C.1), revealed a presence of both fluorite- and bixbyite-type structures which were not distinguished by the conventional XRPD. The fluorite-type structure or structure domain is presumably formed in order to accommodate the excess oxygen necessary to raise the manganese oxidation state above 3. It is hence probable that other compositions of the liquid-mix samples in Tables 2 and 3 have both bixbyite and fluorite domains, especially those with elevated manganese oxidation states.

Temperatures above 690°C

When the temperature is increased above 690°C, the liquid-mix-based solid solutions exsolve hexagonal $ScMnO_3$ leaving a more Sc-, or Mn-rich cubic solid-solution phase. The temperature at which this occurs increases as the scandium content increases. With reference to the melting temperatures of the pure oxides, this is indicative of a process controlled by the diffusion of the metal atoms, hence by kinetic, not thermodynamic factors.

The estimated contents of the chemical phases and their unit-cell parameters are listed in Tables 4 and 5, respectively, for several temperatures, referring to annealings of the inorganic precursors for 48 h in flowing O_2. At the lowest temperature listed, the complete miscibility is maintained; at the highest, the samples apparently assume their thermodynamic equilibrium composition. To support these claims, shorter annealings (24 h) and higher temperatures (1150°C) have been tested (but are not listed in Tables 4 and 5). Of the results listed, only the $x = 0.60$ composition at 750°C appears to be just in the process of the decomposition (Table 4). This shows that the exsolution process is accomplished rapidly in a narrow temperature interval.

The exsolution of $ScMnO_3$ leads to a change in the unit-cell parameter of the bixbyite-type phase, which is most apparent for the $x = 0.4$ and $x = 0.60$ samples closest to $ScMnO_3$. However, the unit-cell parameter of the liquid-mix based samples clearly behaves nonideally as a function of x, owing to both the instability of the $(Sc_{1-x}Mn_x)_2O_{3+\delta}$ solid solutions and the variations in their oxygen contents. Thus the unit-cell parameter a of the bixbyite-type phase in the $x = 0.80$ samples seem to slightly increase after the annealings at increased temperatures, despite the exsolution of $ScMnO_3$. This is apparently due to the occurring redox change, viz. the volume increase due to the decrease of the manganese oxidation state to $+3$, stable in the well-crystalline solid solution, as compared to the oxygen-rich samples with high disorder. The unit-cell parameters are hence not suitable for composition estimates.

The compositions of the stable bixbyite-type solid solutions formed under exsolution of $ScMnO_3$ at high temperatures were therefore balanced from the estimated contents of the chemical phases listed in Table 4. The resulting Mn contents (Table 6) are surprisingly consistent, considering the possible errors of the phase-content estimates. The stable bixbyite-type solid solution gradually develops from the liquid-mix solid solution as a separate phase by precipitation of $ScMnO_3$, shifting its composition towards the apparently stable value x_{lim}. As the quantitative phase-fraction analysis is more precise when the $ScMnO_3$ content is low, reasonable estimates for the solid-solution limits are around $x_{lim} = 0.15$ and $x_{lim} = 0.90$ for the Sc- and Mn-rich phases, respectively, after being freely cooled from 1000°C in O_2.

TABLE 5

Exsolution of Hexagonal ScMnO$_3$ from Cubic Liquid-Mix (Sc$_{1-x}$Mn$_x$)$_2$O$_{3+\delta}$ at Temperature t under a 48-h Annealing in 1 atm O$_2$: Unit-Cell Parameters a, c (in Å)^a

t (°C)	$x = 0.20$		$x = 0.40$		$x = 0.60$		$x = 0.80$	
	Cubic	ScMnO$_3$	Cubic	ScMnO$_3$	ScMnO$_3$	Cubic	ScMnO$_3$	Cubic
690 a	9.783(5)		9.693(4)		9.583(2)		9.442(2)	
750 a	9.787(4)		9.695(4)		5.822(4)	9.580(1)	5.827(1)	9.450(1)
c					11.180(7)		11.192(4)	
850 a	9.787(3)		9.774(4)	5.8312(6)	5.825(1)	9.471(7)	5.8315(9)	9.4530(7)
c				11.187(2)	11.179(4)		11.197(2)	
1000 a	9.7885(8)	5.8348(8)	9.800(6)	5.8336(6)	5.8270(7)	9.4686(5)	5.8273(15)	9.4613(5)
c		11.185(1)		11.178(2)	11.172(2)		11.176(3)	

^{a} Sc$_2$O$_3$ under analogous conditions: $a = 9.8474(5)$ Å; Mn$_2$O$_3$: $a = 9.4109(13)$ Å.

B. Ordering of the Liquid-Mix ScMnO$_{3+\delta}$

Whereas in general the cubic liquid-mix solid solutions (Sc$_{1-x}$Mn$_x$)$_2$O$_{3+\delta}$ decompose under exsolution of ScMnO$_3$ into two-phase mixtures, the composition $x = 0.50$ yields a pure hexagonal ScMnO$_3$. This change from disorder to order was studied as a function of time and temperature. Series of pellets made from the 690°C master sample with $x = 0.5$ were annealed in a flowing atmosphere of O$_2$ and air at several temperatures, and the individual samples were taken from the furnace into air and rapidly quenched on a metal surface after the desired value of time had expired. The phase content was then determined by conventional XRPD. An external calibration method was used for these estimates. The standard of the cubic liquid-mix phase was obtained by annealing the 690°C master sample for an additional 10 h at 700°C in flowing O$_2$, the standard for the hexagonal phase was obtained from the same master sample at 900°C after 36 h in the same atmosphere. The calibration samples contained 0, 10, 20, … , 100 wt% of the standard phases next to each other and were mixed with 140 wt% of Si to assure that the total amount of ScMnO$_3$ in the XRPD sample is constant. The same was done with the annealed samples, and their phase content was determined from the intensity ratios of selected vicinal pairs of Bragg reflections of the present phases: hexagonal (111, 004, 300) and cubic (222, 440; referring to the bixbyite-type cell). For several reasons which generally affect the Bragg-line intensities of the XRPD photographs, the obtained quantitative data are only approximate and their standard error can be estimated to be at least 10 to 20% of the value.

Despite all of the deviations included, the experimental data provide a reasonably consistent picture of the ordering reaction. The product formation follows a simple exponential at the low-temperature end of the relevant region, whereas, at higher temperatures, an induction period is clearly seen. This is an indication that two processes with

possibly two time dependencies may be involved, and these are assumed to be a nucleation and a transport or chemical reaction. The somewhat scattered S-shaped curves can be fitted by various empirical equations, but a simplification was chosen which describes these two processes as two subsequent homogeneous reactions,

$$c \xrightarrow{k_1} N \xrightarrow{k_2} h, \qquad [3]$$

where c and h denote the cubic and hexagonal ScMnO$_3$ phases and N denotes the crystallization nuclei (k_1 and k_2 are rate constants). This approach is believed to have some anchoring in the actual physical system, given the nanoscale nature of the initial powder component and its morphology in relation to the foamed organic precursor which has a high proportion of two- and one-dimensional linkages. Originating at zero (unity concentration of c), the mass fraction $w_h(\tau)$ of the product h seen by XRPD after time τ is further assumed to refer to the mixture of h and c only, viz., the proportion belonging to N not being visible by XRPD and hence somewhat arbitrarily assigned to the hypothetical nuclei,

$$w_h(\tau) = \frac{x_h(\tau)}{x_h(\tau) + x_c(\tau)} = \eta, \qquad [4]$$

TABLE 6

Mn Contents x' in (Sc$_{1-x}$Mn$_{x'}$)$_2$O$_3$ Formed at Various Temperatures t in O$_2$ (48 h) from the Liquid-Mix (Sc$_{1-x}$Mn$_x$)$_2$O$_{3+\delta}$ Samples under Exsolution of ScMnO$_3$

| t (°C)	$x = 0.20$	$x = 0.40$	$x = 0.60$	$x = 0.80$
750			0.69	0.83
850		0.14	0.98	0.89
1000	0.16	0.12	0.95	0.88
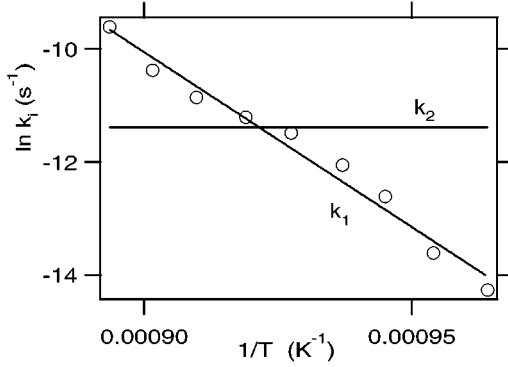
FIG. 1. Disorder–order transition of liquid-mix $ScMnO_3$; Arrhenius-type plot for the rate constant k_1 while k_2 is constant, fixed to the fitted value.

FIG. 2. Disorder–order transition of $ScMnO_3$; extent of reaction η as a function of time τ and temperature. Fitted isotherms are drawn for $t = 846, 836, 826, 815, 805, 794, 785, 775,$ and $764°C$; the latter is dotted.

where $x_c(\tau)$ and $x_h(\tau)$ represent the well-known solutions for molar fractions of c and h in the system of subsequent reactions according to Eq. [3]. The temperature dependences of k_1 and k_2 in the resulting equation for the overall observed extent of reaction η,

$$\eta = \frac{k_1[-1 + \exp(-k_2\tau)] + k_2[1 - \exp(-k_1\tau)]}{k_1[-1 - \exp(-k_1\tau) + \exp(-k_2\tau)] + k_2}, \quad [5]$$

were expressed with Arrhenius equations, but the bivariate fitting in the τ, T space gave best results when the temperature dependence for k_2 was neglected altogether. Three parameters were hence obtained: the preexponential factor $A_1 = 9.58 \times 10^{21}$ s^{-1}, the activation energy $E_{A,1} = 560$ $kJmol^{-1}$ and $k_2 = 1.14 \times 10^{-5}$ s^{-1}. This result is interpreted in that the formation of the stable, ordered high-temperature phase is dictated by the (nucleation) reaction 1 in Eq. [3] which starts when the relatively high activation energy is supplied. Thus step 2 in Eq. [3] could be the actual growth of the product. It does not have a strong temperature dependence, but apparently becomes the rate-controlling factor at high-temperatures. For illustration, the Arrhenius-type plot is shown in Fig. 1 for the rate constant k_1 (while k_2 is constant) and a main portion of the fitted region is shown in Fig. 2.

In addition to the strong approximations associated with the use of Eq. [3], it has also been neglected that a small amount of O_2 must be released from the oxygen-rich solid solution during the ordering reaction, as a consequence of the oxidation state of Mn being exactly trivalent in the ordered, hexagonal $ScMnO_3$. The existence of this redox component means that the ordering of the liquid-mix based solid solution should be promoted by a decrease in the partial pressure of oxygen. Two trial isotherms have therefore been measured in an air atmosphere and indeed found significantly above those valid for O_2 in Fig. 2. The shift corresponds to the temperature difference of some $20°C$.
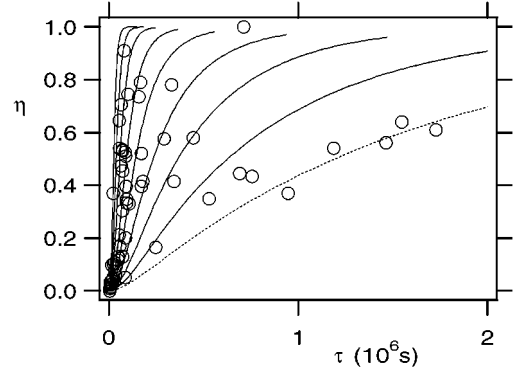
C. Synchrotron XRPD Study of the Liquid-Mix and Ordered ScMnO₃ Phases

Phase composition, crystal structure, size and strain parameters of the crystallites were investigated on both the liquid-mix and ordered $ScMnO_3$ with the help of synchrotron XRPD diffraction. The samples were identical with the calibration standards in Section IIIB, viz., the liquid-mix sample was obtained by a 10-h annealing at $700°C$, the ordered phase by a 36-h annealing at $900°C$, referring to the same master sample and O_2 atmosphere. The products were characterized in the same manner as the other compositions, viz., by determining the overall Mn oxidation state and the formal oxide content in the sample, and assuming that the rest is CO_2 and/or H_2O. The results of these chemical analyses are presented in Table 7.

1. Liquid-Mix ScMnO₃ (700°C)

Visual inspection of the XRPD pattern collected on the $ScMnO_3$ sample prepared at $700°C$ indicated a single-phase bixbyite-type sample with rather broad peaks. However, detailed examinations revealed a more complicated situation. Attempts to model the peak positions using a single

TABLE 7
Compositions of the Liquid-Mix Disordered and Ordered Samples of $ScMnO_{3+\delta}$ Used for Synchrotron XRPD

Sample	δ	v(Mn)	w(oxide)	$n(CO_2)$	$n(H_2O)$
Liquid-mix	0.227(7)	3.45(1)	0.95(1)	0.17(2)	0.42(6)
Ordered	0.003(3)	3.01(1)	0.99(1)	0.04(3)	0.09(8)

Note. Mass fractions w(oxide) of $ScMnO_{3+\delta}$ and moles of residual CO_2, or, alternatively, H_2O, are listed per this formula unit.

lattice constant were unsuccessful. The peaks where all three *hkl* indices were even (subcell peaks) were shifted to higher 2Θ values, while the remainder of the peaks (supercell peaks) were shifted to lower 2Θ values. Further attempts to fit the subcell peaks, most of which were rather strong, revealed that these reflections were actually a convolution of two peaks. Rietveld refinement of the XRPD pattern confirmed the presence of two crystalline phases. The majority phase ($\sim 80\%$) adopts the fluorite structure, while the minority phase ($\sim 20\%$) has the bixbyite structure. Besides the phase fraction, unit-cell and profile parameters associated with each phase, two thermal parameters (one for Sc/Mn and one for oxygen) were refined for both the fluorite- and bixbyite-type phases. Fluorite has no free positional parameters, while bixbyite has one free metal positional parameter (which was refined) and three free oxygen positional parameters (which were fixed to values reported in Ref. (25)). The observed, calculated and difference patterns are shown in Fig. 3. Numerical details of the refinement are listed in Table 8.

The fluorite/bixbyite model explains the unusual features present in the XRPD pattern. Bixbyite can be derived from a $MO_{1.5}\square_{0.5}$ anion-deficient fluorite structure by ordering of the vacancies and relaxation of the oxygen ions, resulting in a doubling of the unit-cell parameter (25). When the cation sublattice is nearly the same for both structures, fluorite peaks will overlap with the strong, all-even-*hkl*, bixbyite peaks in the XRPD pattern. A two-phase fluorite/bixbyite sample would have subcell reflections which contain contributions from both phases, and supercell reflections associated exclusively with the bixbyite structure. Since the fluorite-type structure is the majority phase in the sample, its lattice parameter being smaller than $a/2$ of the bixbyite-type structure explains the apparent shift of the subcell reflections to higher 2Θ values. Considering that an ordered atom assembly is packed more efficiently than a disordered one, this lattice relationship is somewhat unexpected. However, the contraction of the fluorite-type lattice can be explained when the difference in $v(Mn)$ is taken into
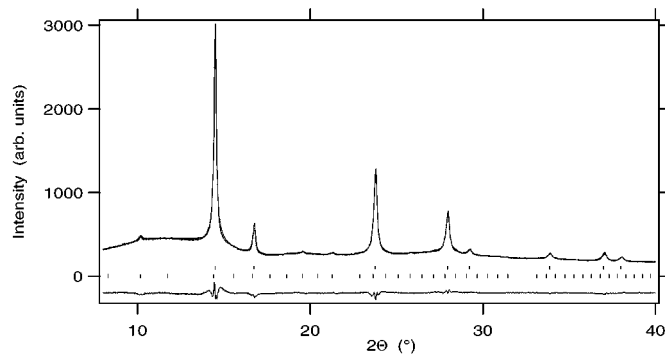

FIG. 3. The observed, calculated, and difference patterns from the Rietveld refinement of the liquid-mix $ScMnO_3$ sample annealed at $700°C$. The observed pattern is represented by dots, while the calculated and difference patterns are drawn in solid lines. The upper set of vertical ticks marks the positions of fluorite peaks, while the lower set of ticks marks the positions of bixbyite peaks.

consideration. Table 7 lists $v(Mn) = 3.45$ and composition $ScMnO_{3.227}$ for the overall sample. Incorporation of the excess oxygen into the bixbyite structure could easily destroy the long range ordering of vacancies, thereby stabilizing the defect fluorite structure. This implies a higher concentration of Mn^{4+} and a corresponding contraction of the lattice parameter in the defect fluorite-type phase, due to the smaller ionic radius of Mn^{4+} (0.53 Å) with respect to Mn^{3+} (0.645 Å) (26, 27). Assuming all manganese ions in the truly bixbyite-type phase are trivalent (stoichiometry $ScMnO_3$) and neglecting any contributions from amorphous phases, one can balance charges to obtain $v(Mn) = 3.58$ and composition $ScMnO_{3.288}$ for the fluorite-type phase.

2. Ordered $ScMnO_3$ ($900°C$)

Several important changes in the structural and compositional makeup of the liquid-mix precursor are induced by annealing at $900°C$ for 36 h. XRPD analysis shows that the

TABLE 8
Rietveld Refinement Results for Liquid-Mix Disordered and Ordered $ScMnO_3$

| Sample | Structure type | Unit-cell parameters (Å, Å³) | | | Mass fraction | Profile coefficients | | | | R_{wp} | R_{F^2} | χ^2 | No. of refl. | 2Θ |
		a	c	V/Z		U	P	X	Y					
Liquid-mix	Bixbyite	9.643(2)		56.04	0.23(3)			14(1)	96(7)	2.77	8.10	11.2	48	8–40°
	Fluorite	4.8091(1)		55.61	0.77			7.4(2)	56(1)					
Ordered	Bixbyite	9.803(1)		58.88	0.024(3)			4	36	4.33	4.16	16.1	416	6.5–65°
	$ScMnO_3$	5.83150(1)	11.17504(4)	54.85	0.976	9.5(8)	2.50(4)	0.69(4)	5.0(2)					
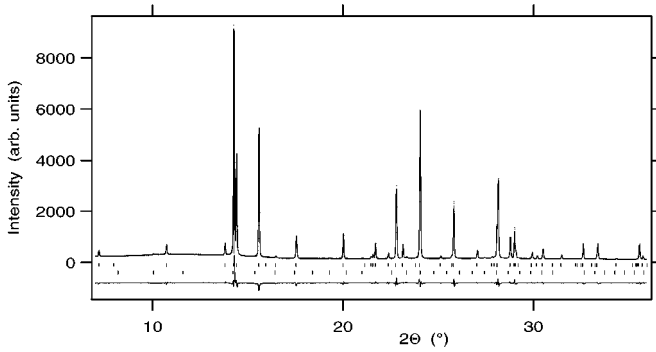
FIG. 4. The observed, calculated, and difference patterns from the Rietveld refinement of the ordered $ScMnO_3$ sample annealed at 900°C. The observed pattern is represented by dots, while the calculated and difference patterns are drawn in solid lines. The upper set of vertical ticks marks the positions of the ordered $ScMnO_3$ peaks, while the lower set of ticks marks the positions of bixbyite peaks.

FIG. 5. The integral breadths of the bixbyite- (circles), fluorite- (diamonds), and ordered-$ScMnO_3$ (triangles), as well as the silicon reference sample (open squares) as functions of 2Θ.

mixture of the fluorite- and bixbyite-type phase, including the possible amorphous content still present after annealing at 700°C, is transformed almost exclusively into the ordered $ScMnO_3$ structure. There is also a small amount (2.5 wt%) of a bixbyite-type phase remaining. Major features of the Rietveld refinement are given in Table 8. The fractional coordinates are not listed, but they show good agreement with the ordered $ScMnO_3$ structure reported in the literature (13). The refined fit to the pattern is illustrated in Fig. 4. Compositionally, the excess oxygen, CO_2 and H_2O present at 700°C have been expelled. This is presumably associated with the disappearance of the fluorite structure, which is known to readily accommodate nonstoichiometry. Finally, the widths of the Bragg peaks have decreased considerably, indicating either an increase in the crystallite size and/or a decrease in the strain. This is discussed in more detail below. The small amount of the bixbyite-type phase present at this temperature has a significantly larger unit cell constant than the phase present in the sample annealed at 700°C. This implies that its stoichiometry has changed from the 1 : 1 ratio at 700°C to a scandium rich composition at 900°C. The presence of such phase in the sample annealed at 900°C is probably a result of a slight deviation from a perfect 1 : 1 scandium to manganese ratio in the precursor. It also illustrates the very limited compositional range over which the ordered $ScMnO_3$ phase is stable.

3. Crystallite Size and Micro-Strain Analysis

Peak broadening in X-ray or neutron powder diffraction can be attributed to one or more of the following sources: instrumental broadening, finite crystallite size, the presence of micro-strain and/or extended defects (stacking faults, micro-twinning, dislocations, etc.) (28). Analysis and deconvolution of the peak broadening can give important
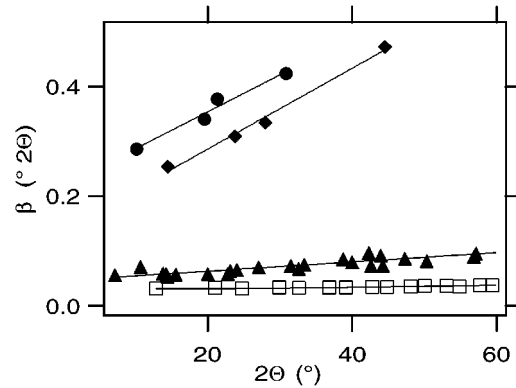
information regarding the microstructure and morphology of a sample. As mentioned in the preceding section, the ordered $ScMnO_3$ phase present after annealing at 900°C has much sharper Bragg peaks than either the fluorite- or bixbyite-$ScMnO_3$ present in the sample annealed at 700°C. Since the instrumental configuration used in data collection was identical for the two samples, a change in the microstructure/morphology is implied. To illustrate the magnitude of this effect, integral breadths β, for ordered-, bixbyite-, and fluorite-$ScMnO_3$ are plotted versus 2Θ in Fig. 5. In addition, β values from a sample of crushed silicon crystals, analyzed using the same instrumental configuration, are also included in Fig. 5. Because the silicon sample has very large and strain-free crystallites, the broadening observed for this sample represents the instrumental contribution to the peak broadening. Figure 5 clearly shows that all three $ScMnO_3$ phases contain peak-broadening contributions from the sample and that these contributions are much smaller in the ordered $ScMnO_3$ phase than in the other two phases. Furthermore, no anisotropic *hkl*-dependent peak-broadening effects are present. This allows one to estimate the peak broadening as a convolution of isotropic crystallite size and micro-strain effects.[1]

When the Bragg reflections have a Lorentzian peak shape, the possible peak broadening effects add in a linear fashion:

$$\beta = \beta_{\text{size}} + \beta_{\text{strain}} + \beta_{\text{instr}}. \qquad [6]$$

---

[1] The absence of anisotropic broadening implies that extended defects, if they are present, must have a random orientation. Randomly oriented extended defects would only act to separate crystalline domains and reduce the average crystallite size. The distinction between crystallites separated by dislocations/defects and crystallites belonging to different particles is not one that can be made using powder diffraction methods.

Both the size and strain contributions have angular dependences. The former is given in Eq. [2], the latter is expressed via Eq. [7] for the occurring strain (micro-deformation) of the interplanar distances, $\varepsilon = \Delta d/d$, as [29]

$$\varepsilon = \beta_{strain}/(4\tan\Theta), \qquad [7]$$

where β_{strain} is in radians 2Θ. After insertion into Eq. [6] and rearrangement, a dimensionless function of the broadening is obtained,

$$(\beta_i - \beta_{instr})\cos\Theta_i = \frac{\lambda}{D_v} + 4\varepsilon\sin\Theta_i, \qquad [8]$$

where β_i is the integral breadth (in radians 2Θ) of the ith Bragg reflection positioned at $2\Theta_i$. This function is the basis for the Williamson–Hall (W–H) plot which is used to quantify crystallite size and strain contributions to peak broadening (22, 28, 30, 31).

The peak profiles for both phases in the liquid-mix sample are essentially pure Lorentzian, making the W–H analysis quantitative. However, the peak profiles for the ordered $ScMnO_3$ phase and the silicon reference sample have a Gaussian component, and for this, the following equations are applicable (32):

$$\beta^2 = \beta_{size}^2 + \beta_{strain}^2 + \beta_{instr}^2, \qquad [9]$$

$$(\beta^2 - \beta_{instr}^2)\cos^2\Theta_i = \left(\frac{\lambda}{D_v}\right)^2 + 16\varepsilon^2\sin^2\Theta_i. \qquad [10]$$

Therefore, in order to properly analyze the ordered $ScMnO_3$ sample, the Lorentzian and Gaussian peak-broadening contributions were analyzed separately. The Lorentzian and Gaussian integral breadths, β_{Lor} and β_{Gauss}, were determined using the method suggested by Delhez et al. (28), and are plotted as a function of 2Θ in Fig. 6 for both ordered $ScMnO_3$ and silicon. Notice that in both cases β_{Gauss} are essentially angle independent. This behavior would be expected if the Gaussian broadening was simply a consequence of the non-infinitesimal diameter of the sample contained in the capillary. In order to test this possibility, a simple geometric argument has been adopted which predicts that such a contribution to the peak broadening would have a magnitude of

$$\beta_{cap} = \frac{360 d_{cap}}{2\pi r}, \qquad [11]$$

where d_{cap} is the capillary diameter and r is the distance from the capillary to the detector. Given that $r = 450$ mm and inserting the appropriate values of $d_{cap} = 0.21$ mm for the silicon sample and $d_{cap} = 0.38$ mm for the ordered
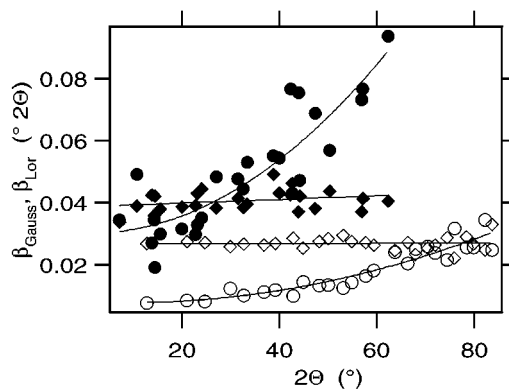

FIG. 6. The Gaussian (diamonds) and Lorentzian (circles) integral breadth components, β_{Gauss} and β_{Lor} for silicon (open symbols) and ordered-$ScMnO_3$ (filled symbols). Gaussian components are fitted linear; Lorentzian components are fitted using a second degree polynomial.

$ScMnO_3$ sample, $\beta_{cap}(Si) = 0.027°$ and $\beta_{cap}(ScMnO_3) = 0.048°$ (in 2Θ) are obtained, in reasonable agreement with the values of the Gaussian components in Fig. 6. The Gaussian peak-broadening component is therefore considered to be a consequence of the finite capillary diameter and hence neglected. The instrumental contribution to peak broadening is then empirically estimated from the silicon data to be

$$\beta_{instr} \approx \beta_{Lor}(Si) = 0.0081 - \frac{\Theta}{7375} + \frac{\Theta^2}{62500}. \qquad [12]$$

Combining Eqs [8] and [12], a W–H analysis of the peak broadening in ordered, bixbyite-, and fluorite-type $ScMnO_3$ can be carried out. The W–H plot is shown in Fig. 7 and the evaluated D_v and ε parameters are listed in Table 9.

Crystallite size and micro-strain parameters can also be estimated from the profile parameters contained in the GSAS refinement (20). The profile parameters U, V, W, P, X, and Y are used in GSAS to describe the dependence of
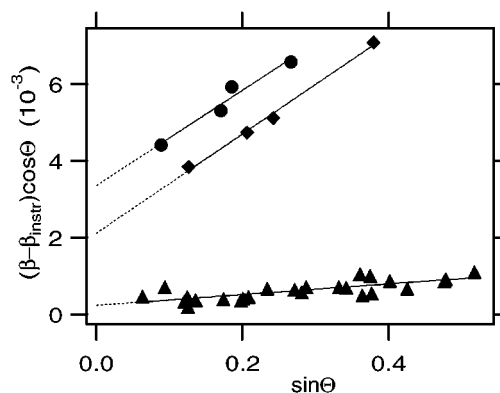

FIG. 7. Williamson–Hall plots for the bixbyite- (circles), fluorite- (diamonds) and ordered-$ScMnO_3$ (triangles).

TABLE 9
Crystallite Size D_v (in Å) and Micro-Strain ε (in %) for the Fluorite- and Bixbyite-Type Phases Present in the Liquid-Mix Disordered ScMnO$_3$ and for the Ordered ScMnO$_3$ Sample

Sample	Structure type	W–H		Rietveld	
		D_v	ε	D_v	ε
Liquid-mix	Fluorite	330	0.32	345	0.38
	Bixbyite	202	0.31	183	0.66
Ordered	ScMnO$_3$	2920	0.03	3710	0.02

the full-width-at-half-maximum (on the 2Θ scale, in centidegrees) as a function of Θ. If V and W are set to zero, the refined values of U, P, X, and Y can be used to estimate both Gaussian and Lorentzian values of D_v and ε. Equations are given in the GSAS manual for calculating crystallite size and micro-strain, however, in order to obtain quantitatively meaningful values these equations need to be modified to express peak broadening in terms of integral breadths rather than FWHM's, and the factor of 4 which proceeds the strain-broadening term must be included. Incorporating these modifications gives

$$D_v(\text{Lor}) = \frac{36000\lambda}{\pi^2 X}, \qquad [13]$$

$$\varepsilon(\text{Lor}) = \frac{\pi^2(Y - Y_{\text{instr}})}{144000}, \qquad [14]$$

and

$$D_v(\text{Gauss}) = 18000\frac{\lambda}{\sqrt{2\pi^3 P}}, \qquad [15]$$

$$\varepsilon(\text{Gauss}) = \frac{\sqrt{2\pi^3(U - U_{\text{instr}})}}{72000}, \qquad [16]$$

where λ is the wavelength and $Y_{\text{instr}}/U_{\text{instr}}$ are obtained from refinement of the line-broadening reference sample. The D_v and ε values obtained using the Rietveld (GSAS) method are listed in Table 9, showing a good agreement with the W–H technique. This indicates that a reasonably accurate size/strain analysis can be obtained from the GSAS profile parameters, using Eqs [13]–[16]. However, it should be noted that no allowance is given in GSAS for subtracting the instrumental contribution from the crystallite size terms, X and P. This may lead to larger discrepancies between the Rietveld and W–H techniques in cases when the instrumen-

tal peak-broadening contribution is substantial, for example when the crystallite size is relatively large. Such a problem is probably responsible for the difference in the size values obtained for the ordered ScMnO$_3$, whereas the notable difference between the strain values for the bixbyite-type phase may be the consequence of the way in which the overlapping fluorite/bixbyite peaks are deconvoluted. In the former case the W–H analysis should be more accurate, whereas in the latter case the Rietveld approach may well be more accurate.

The results given in Table 9 indicate that ordering of scandium and manganese cations results in an order of magnitude decrease in the strain, accompanied by an order of magnitude increase in the crystallite-size. The highly strained lattices observed for both bixbyite- and fluorite-ScMnO$_3$ are undoubtedly a consequence of the fairly large difference that exists in ionic radii of trivalent scandium (0.745 Å) and manganese (0.645 Å) (26, 27). The excessive strain present in these compounds may necessitate a high concentration of dislocations, defects, and/or surfaces which would limit the maximum crystallite size which can be attained. Annealing at higher temperatures increases the diffusion of ions allowing scandium and manganese to order, which in turn dramatically reduces the strain. Both the increased diffusivity of ions and the reduced strain favor crystallite growth, explaining the much larger crystallite size observed in ordered ScMnO$_3$ after annealing at 900°C.

IV. DISCUSSION

The fact that the liquid-mix-based solid solution $(\text{Sc}_{1-x}\text{Mn}_x)_2\text{O}_{3+\delta}$ exists at low temperatures throughout the entire composition range speaks for its being a metastable remnant of the liquid mixing. However, the synchrotron XRPD experiment for the $x = 0.50$ composition shows that there is another important stabilization factor, oxidation. This redox contribution is manifested in the formation of the fluorite-type phase ScMnO$_{4-v}$ occurring together with the closely related bixbyite-type solid solution ScMnO$_3$. This suggests that a similar (entropy) stabilization by the excess oxygen and the carbonate and/or hydroxide ions occurs across this solid solution series, in line with the variations in the oxygen content parameter δ.

Disordered variants of ordered structures have also been obtained for other systems at low temperatures, when using the liquid-mix citrate synthesis route. As an example, YBa$_2$Fe$_3$O$_8$ is formed as a cubic perovskite-type phase below some 900°C, and orders into the triple-perovskite-type at higher temperatures (33). Also other low-temperature syntheses lead to products stabilized by the limited diffusion, like sol-gel alkoxide techniques (34, 35), spray-pyrolysis (36), and coprecipitation (6) methods.

In all these syntheses of multicomponent oxides, the random distribution of the metal atoms is retained in both the

precursor and the crystalline product, regardless the normally observed thermodynamic solid-solubility limits for the pure oxide phase. For a given, chemically suitable partial pressure of oxygen, the critical condition is the temperature. To obtain a metastable disordered phase, the kinetics must favor formation of such a phase from the precursor over both phase segregation and diffusional redistribution of metal atoms into an ordered arrangment, as illustrated for $ScMnO_3$. In this case, the solid solution adopts the structure type of the end-member binary oxides, in other cases like $YBa_2Fe_3O_8$ in Ref. (33), a simple structural arrangement is formed based on dense packing of the oxide anions, with substitutional disorder at the metal sites. When the metals ratio falls outside the thermodynamic solid solubility limits, the disordered liquid-mix phase transforms into an ordered structure plus a stable solid solution when the activation energy is supplied. Having originated in an atomically mixed disordered state, this process is reminiscent of the Ostwald step rule. The process of formation of liquid-mix structures with partial conservation of the *amorphous* nature of the precursor can also be regarded as a special case of topotactical reactions, where the segments which persist into the reaction products are not those of a structural order but those of a structural disorder.

ACKNOWLEDGMENTS

REFERENCES

1. R. Roy, *J. Mater. Edu.* **18,** 267 (1996).
2. M. P. Pechini, US Patent 3,330,697 (1967).
3. P. Karen and A. Kjekshus, *J. Am. Ceram. Soc.* **77,** 547 (1994).
4. P. Barboux, P. Griesmar, F. Ribot, and L. Mazerolles, *J. Solid State Chem.* **117,** 343 (1995).
5. E. Rossen, J. N. Reimers, and J. R. Dahn, *Solid State Ionics* **62,** 53 (1993).
6. A. Rousset, *Solid State Ionics* **63–65,** 236 (1993).
7. L. N. Komissarova, B. I. Pokrovskii, and I. S. Shaplygin, *Izv. Akad. Nauk. SSSR Neorg. Mater.* **2,** 275 (1966).
8. T. Atsumi, T. Ohgushi and N. Kamegashira, *J. Alloys Compds.* **238,** 35 (1996).
9. S. Geller, P. Romo, and J. P. Remeika, *Z. Kristallogr.* **126,** 461 (1968).
10. S. Geller and G. P. Espinosa, *Phys. Rev. B: Condens. Matter* **1,** 3763 (1970).
11. S. Geller, *Acta Crystallogr. Ser. B* **27,** 821 (1971).
12. R. Norrestam, *Acta Chem. Scand.* **19,** 1009 (1965).
13. J. E. Greedan, M. Bieringer, J. F. Britten, D. M. Giaquinta, and H.-C. zur Loye, *J. Solid State Chem.* **116,** 118 (1995).
14. I. O. Troyanchuk and V. N. Derkachenko, *Sov. Phys. Solid State* **30,** 2003 (1988).
15. J. E. Greedan, N. P. Raju, and M. A. Subramanian, *Solid State Commun.* **99,** 399 (1996).
16. P. E. Werner, "The Computer Programme SCANPI 9." Institute of Inorganic Chemistry, University of Stockholm, Sweden, 1992.
17. K. Yvon, W. Jeitschko, and E. Parthé, *J. Appl. Cryst.* **10,** 73 (1977).
18. J. Fiala, *Silikaty* **29,** 273 (1985).
19. G. C. Smith, *Synchrotron Rad. News* **4,** 24 (1991).
20. A. C. Larson and R. B. Von Dreele, "GSAS: General Structural Analysis System." Los Alamos National Laboratory, Los Alamos, NM, 1994.
21. P. Scherrer, *Nachr. Ges. Wiss. Gottingen, Math.-Phys. Kl.* **2,** 96 (1918).
22. S. A. Howard and K. D. Preston, "Modern Powder Diffraction," Reviews in Mineralogy, Vol. 20, Chap. 8 (D. L. Bish and J. E. Post, Eds.). Mineralogical Society of America, Washington, DC, 1989.
23. J. I. Langford, *J. Appl. Cryst.* **11,** 10 (1978).
24. G. Malmros and J. O. Thomas, *J. Appl. Crystallogr.* **10,** 7 (1977).
25. F. Galasso, "Structure and Properties of Inorganic Solids," pp. 99–102 Pergamon, Oxford/New York, 1970.
26. R. D. Shannon, *Acta Crystallogr., Ser. A* **32,** 751 (1976).
27. R. D. Shannon and C. T. Prewitt, *Acta Crystallogr., Ser. B* **25,** 925 (1969).
28. R. Delhez, T. H. de Keijser, J. I. Langford, D. Louër, E. J. Mittemeijer, and E. J. Sonneveld, "The Rietveld Method," IUCr Monograph on Crystallography No. 5, Ch. 8 (R. A. Young, Ed.), Oxford Univ. Press, Oxford, 1993.
29. A. R. Stokes and A. J. C. Wilson, *Proc. Phys. Soc. London* **56,** 174 (1944).
30. G. K. Williamson and W. H. Hall, *Acta Metallurg.* **1,** 22 (1953).
31. J. I. Langford, D. Louër, E. J. Sonneveld, and J. W. Visser, *Powder Diffraction* **1,** 211 (1986).
32. D. Balzar and S. Popovic, *J. Appl. Cryst.* **29,** 16 (1996).
33. P. Karen, P. H. Andresen, and A. Kjekshus, *J. Solid State Chem.* **101,** 48 (1992).
34. F. F. Lange, M. L. Balmer, and C. G. Levi, *Sol–Gel Sci. Technol.* **2,** 317 (1994).
35. L. Bonhomme-Coury, N. Lequeux, S. Mussote, and P. Boch, *Sol–Gel Sci. Technol.* **2,** 371 (1994).
36. T. González-Carreño, M. P. Morales, and C. J. Serina, *J. Mater. Sci. Lett.* **13,** 381 (1994).